catalysts

MDPI

Article

Preparation of Mn-Doped Co_3O_4 Catalysts by an Eco-Friendly Solid-State Method for Catalytic Combustion of Low-Concentration Methane

Linshuang Xue [1], Chenyi Yuan [1], Shipeng Wu [1], Zhen Huang [1,*], Zhen Yan [2], Stéphane Streiff [2], Hualong Xu [1] and Wei Shen [2,*]

[1] Shanghai Key Laboratory of Molecular Catalysis and Innovative Materials, Laboratory of Advanced Materials and Collaborative Innovation Center of Chemistry for Energy Materials, Department of Chemistry, Fudan University, Shanghai 200433, China
[2] Eco-Efficient Products and Processes Laboratory (E2P2L), UMI 3464 CNRS-Solvay, Shanghai 201108, China
* Correspondence: huangzhen@fudan.edu.cn (Z.H.); wshen@fudan.edu.cn (W.S.)

Abstract: Coalbed methane is a significant source of methane in the atmosphere, which is a potent greenhouse gas with a considerable contribution to global warming, thus it is of great importance to remove methane in coalbed gas before the emission. Exploring the economical non-noble metal catalysts for catalytic methane combustion (CMC) has been a wide concern to mitigate the greenhouse effect caused by the emitted low-concentration methane. Herein, a series of Mn-doped Co_3O_4 catalysts have been synthesized by the environmentally friendly solid-state method. As a result, the $Mn_{0.05}Co_1$ catalyst performed the best CMC activity (T_{90} = 370 °C) and good moisture tolerance (3 vol% steam). The introduction of an appropriate amount of manganese conduced Co_3O_4 lattice distortion and transformed Co^{3+} to Co^{2+}, thus producing more active oxygen vacancies. $Mn_{0.05}Co_1$ exhibited better reducibility and oxygen mobility. In situ studies revealed that methane was adsorbed and oxidized much easier on $Mn_{0.05}Co_1$, which is the crucial reason for its superior catalytic performance.

Keywords: active oxygen; catalytic combustion; low-concentration; methane; Mn-Co_3O_4; solid-state

Citation: Xue, L.; Yuan, C.; Wu, S.; Huang, Z.; Yan, Z.; Streiff, S.; Xu, H.; Shen, W. Preparation of Mn-doped Co_3O_4 catalysts by an eco-friendly solid-state method for catalytic combustion of low-concentration methane. *Catalysts* **2023**, *13*, 529. https://doi.org/10.3390/catal13030529

Academic Editors: Juan José Rueda-Márquez, Javier Moreno-Andrés and Irina Levchuk

Received: 29 January 2023
Revised: 25 February 2023
Accepted: 3 March 2023
Published: 5 March 2023

1. Introduction

Methane (CH_4) is one of the most significant greenhouse gases (GHG), whose global warming potential is about 25 times over a 100-year time horizon and about 72 times over a 20-year time horizon than that of CO_2, thus the direct emission of methane can cause a series of severe environmental issues [1,2]. There are many sources of CH_4 in the atmosphere including biogenic, geogenic, and anthropogenic sources. As the main ingredient of natural gas, one of the largest anthropogenic emissions of CH_4 comes from the coal mining process [3,4]. This part of CH_4 is further diluted to 0.1–1.0% after mixing with air during underground mining, resulting in low-concentration coalbed methane. According to the requirements of relevant environmental protection policies, CH_4 emissions need to be strictly controlled. Catalytic methane combustion (CMC) helps to reduce the emission of CH_4 to meet the increasingly strict regulations on emissions reduction [5,6]. Therefore, it is of great significance to develop efficient CMC catalysts. Furthermore, the activation of the methane C–H bond in the gas phase usually requires a very high temperature due to the high stability of the molecular structure [7]. As a result, it is necessary to further optimize the low-temperature activity and thermal stability of CMC catalysts, which is in favor of industrial development and environmental protection.

Noble metal catalysts of Pd, Pt, and Rh are enriched with high activity for the catalytic combustion of low-concentration methane, but their industrial applications are

restricted due to their low thermal stability, the shortage of resources, and high expense of the raw materials [8–10]. Considering cost control and the easy availability of raw materials, transition metal (Mn, Fe, Co, Ni, Cu, *etc.*) oxides are thought to be a feasible substitution for noble metal catalysts as they are prone to realize redox cycles among different oxidation states [9]. The commonly used transition metal oxide catalysts include MnO_x [11–13], Co_3O_4 [5,6,14], CeO_2 [15], NiO [16], and their mixed components [17–22]. A lot of research has proven that Co_3O_4 is one of the most promising transition metal oxides among different CMC catalysts [23,24]. Adding dopants of Ce, Zr, and Mn with higher redox advantages can further enhance catalytic activity by introducing lattice defects and increasing active oxygen species. Specifically, the enhancing effect of Mn is the most remarkable [25–27]. As for Mn–Co composite oxides, different procedures of hydrothermal, co-precipitation, and sol–gel methods are commonly applied to introduce dopants into the support structure. Chang et al. [28] elucidated that the introduction of Mn can promote the formation and mobility of active oxygen as well as the redox cycle between Mn^{4+}/Mn^{3+} and Co^{2+}/Co^{3+}, accelerating the deeper transformation from intermediates to CO_2 and H_2O.

The synthesis method plays a significant impact on the catalytic performance of transition metal oxide catalysts. Compared with the methods above-mentioned, the solid-state method with simple procedures and easily accessible precursors is quite promising in industrial applications. Moreover, no organic solvent is needed in the preparation process with no harmful wastewater emission [29–31]. Akbari et al. [32] ground the nitrates of Mn and Ba into a paste, resulting in a BaO-doped solid-state mixing catalyst. The decent elemental doping under the solid-state method promoted a favorable regulation of the redox property and bi-component synergistic effect of the catalyst, providing more active oxygen for the reaction [33]. However, the emission of nitrogen oxides (NO_x) is still a problem when nitrates are used as precursors. Synthesizing composite oxides by the solid-state method using carbonates as precursors is a green route without wastewater and exhaust gas. However, the application of this method in CMC catalyst preparation has not been reported.

In this work, a solid-state method with carbonates as precursors was applied to investigate the CMC activities of a series of Mn-doped Co_3O_4 catalysts (Mn-Co_3O_4). This method is environmentally friendly with no wastewater or harmful gas emissions. Various characterization measures were applied to investigate the effect of Mn doping on the chemical state of active components, redox properties, and catalytic performance. Adjusting the Mn doping amount to 5.0% not only resulted in the formation of a Co–Mn solid solution and lattice defects, but also modified the surface properties and increased the active oxygen species of Co_3O_4, which was found to be beneficial for improving the catalytic performance. The cost of a prepared $Mn_{0.05}Co_1$ catalyst was lower than that of noble metals, and it has the advantages of high catalytic activity and good water resistance, so it has a good prospect of industrial application.

2. Results and Discussion

2.1. Structural and Textural Properties

The morphologies and microstructures of Co_3O_4, MnO_x, and the synthesized Mn_xCo_1 (x = 0.025, 0.05, and 0.1) catalysts were characterized by SEM and HRTEM. Pure Co_3O_4 (Figure 1a–c) mainly exhibited spherical and polygonal nanostructures with a diameter of 30–50 nm. On doping a low amount of Mn into Co_3O_4, the morphologies and crystal sizes of the obtained $Mn_{0.025}Co_1$ (Figure 1d–f), $Mn_{0.05}Co_1$ (Figure 1g–i), and $Mn_{0.1}Co_1$ (Figure 1j–l) catalysts became irregular with a wider size distribution (10–50 nm). Moreover, the catalyst edges became rougher and more blurred after Mn doping, implicating that the growth of the crystallite had been restrained and the amount of crystal defects increased. Generally, the formation of crystal defects facilitates the formation of more reactive sites and oxygen vacancies for CMC, thus enhancing the combustion activity of the Mn–Co catalyst [34]. Pure MnO_x (Figure 1m–o) showed a random accumulation of worm-like

nanograins (20–50 nm). Clear lattice stripes of all catalysts can be seen in the HRTEM photos, indicating a high crystallinity.

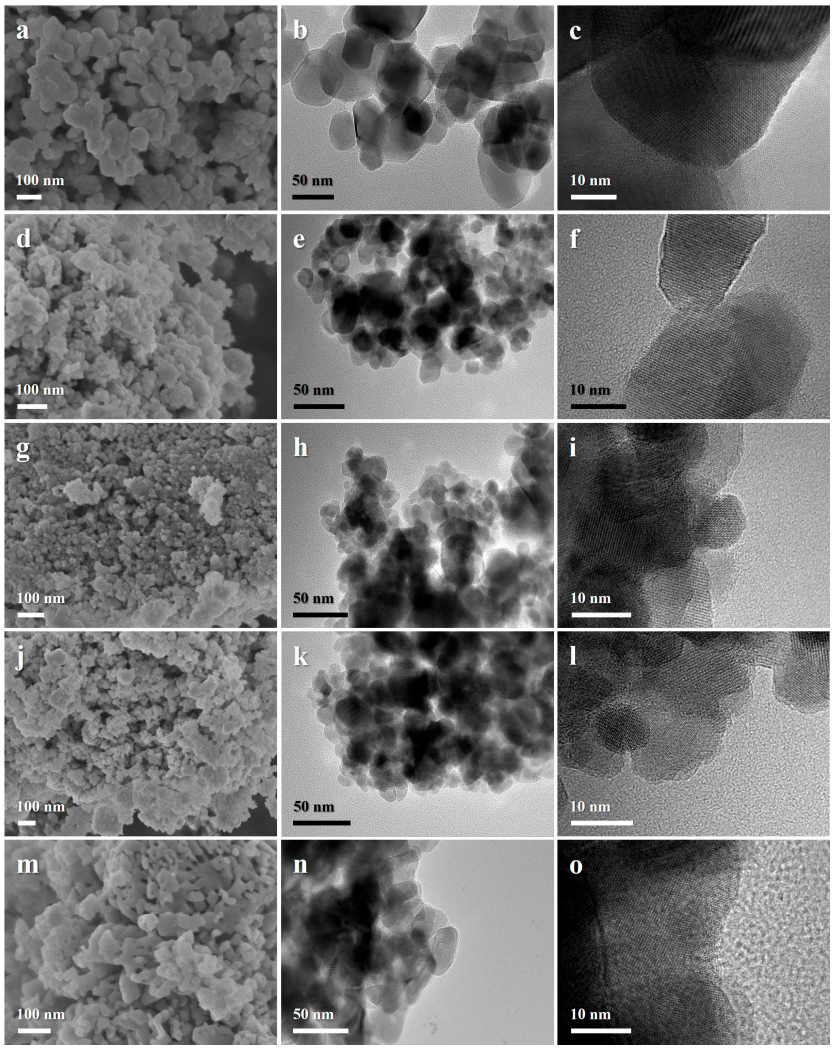

Figure 1. SEM and HRTEM images of Co_3O_4 (**a–c**), $Mn_{0.025}Co_1$ (**d–f**), $Mn_{0.05}Co_1$ (**g–i**), $Mn_{0.1}Co_1$ (**j–l**), and MnO_x (**m–o**) catalysts.

The crystalline phase structures of Co_3O_4 and Mn_xCo_1 were characterized by XRD (Figure 2A). The Mn_xCo_1 catalysts mainly exhibited the characteristic diffraction peaks of Co_3O_4 (JCPDS No. 42-1467), and almost no obvious characteristic diffraction peaks of MnO_x were observed in the XRD patterns, except for the $Mn_{0.1}Co_1$ catalyst, which may be the result of the incorporation of Mn into the Co_3O_4 lattice to form a solid solution or the high dispersion of Mn on the surface of Co_3O_4 [28]. The main diffraction peaks of the Mn-Co_3O_4 catalysts were exposed at 2θ = 19.0°, 31.3°, 36.8°, 38.7°, 44.8°, 55.8°, 59.4°, and 65.2°, which can be attributed to the (111), (220), (311), (222), (400), (422), (511), and (440) facets of the Co_3O_4 phase [35–37]. With the increase in the Mn doping amount to 10.0 mol%, weak diffraction peaks at around 2θ = 33.0° and 55.0° were observed on the $Mn_{0.1}Co_1$ catalyst, which were well-matched with the characteristic diffraction peaks of the Mn_2O_3 (JCPDS No. 41-1442) and Mn_3O_4 (JCPDS No. 04-0732) phases, respectively. This indicates that increasing the Mn doping amount to a certain extent will lead to the formation of some Mn_2O_3 and Mn_3O_4 oxides instead of producing a Mn–Co solid solution. When the doping amount of Mn increased, the intensity of the diffraction peak slightly decreased, while the half-peak width slightly rose, resulting in a gradual reduction in the crystal size. The crystal sizes of the prepared catalysts were calculated by the Scherrer equation (Table

1) in which the mean crystal sizes decreased from 34 nm to 25 nm with an increasing Mn doping amount, which is consistent with the microscope images. Smaller crystals may also boost the formation of low-coordinated defect sites that can promote catalyst activities including surface oxygen vacancies [34]. Based on Mars–van-Krevelen (MvK) mechanisms, the surface-active oxygen species play a decisive role in CH_4 oxidation, providing more assistance for acceleration of the chemical reactions [38]. In addition, the diffraction peak of the Co_3O_4 (311) facet at 36.8° (Figure 2B) gradually shifted toward lower angles, and the corresponding lattice constant (Figure 2C) increased from 8.0608 Å (Co_3O_4) to 8.0809 Å ($Mn_{0.05}Co_1$), with a maximum increase of 0.25%. Considering the crystal radius of Co^{3+} (0.685 Å), which is lower than that of Mn^{3+} (high spin, 0.785 Å; low spin, 0.72 Å), substituting Mn^{3+} for Co^{3+} can result in the expansion of interplanar spacing [39]. Therefore, the shift in the diffraction position and the increase in the lattice constant can be ascribed to the incorporation of Mn ions. Furthermore, incorporating Mn ions also led to the accompanying transformation from Co^{3+} into Co^{2+} [25,40,41]. All of the mentioned changes directly prove that the doped Mn had been incorporated into the Co_3O_4 lattice and a Mn–Co solid solution formed. However, further increasing the doping amount to 10.0% ($Mn_{0.1}Co_1$) resulted in a slight decrease in the lattice constant, indicating no further incorporation of Mn into the Co_3O_4 lattice and no further formation of the Mn–Co solid solution.

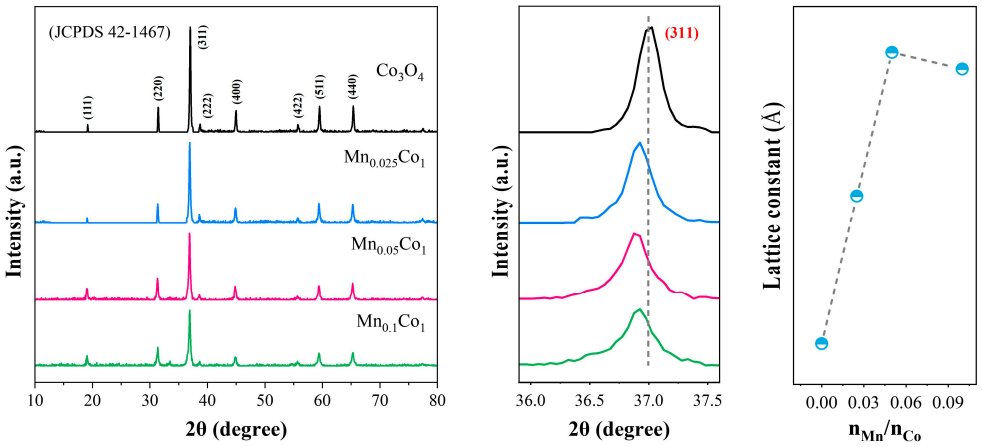

Figure 2. Wide-angle (**a**) and enlarged (**b**) XRD spectra of the Co_3O_4 and Mn_xCo_1 (x = 0.025, 0.05, 0.1) catalysts and (**c**) a variation in the lattice constant of Co_3O_4 as a function of the mole ratio of Mn/Co.

Table 1. Textual properties of the as-obtained catalysts.

Catalyst	Crystallite Size [1] (nm)	Specific Surface Area [2] ($m^2 \cdot g^{-1}$)	Pore Volume [3] ($cm^3 \cdot g^{-1}$)	Average Pore Diameter [4] (nm)
Co_3O_4	34	14	0.09	39.7
$Mn_{0.025}Co_1$	30	26	0.20	28.8
$Mn_{0.05}Co_1$	27	33	0.21	15.6
$Mn_{0.1}Co_1$	25	39	0.21	11.0
MnO_x	28	28	0.22	20.5

[1] Calculated from the line broadening of diffraction peaks by the Scherrer equation from XRD patterns. [2] Determined by the BET method. [3] Total pore volume adsorbed at P/P_0 = 0.99. [4] Determined by the BJH method.

The textual properties of the prepared Co_3O_4, Mn_xCo_1, and MnO_x samples were characterized by N_2 adsorption–desorption isotherms. Figures S1 and S2 illustrate the isotherms and the pore size distributions of the catalysts, respectively. Detailed data about

the specific surface areas, pore volumes, and mean pore sizes of the catalysts are listed in Table 1. Compared with pure Co_3O_4, the Mn-Co_3O_4 catalysts possess a larger specific surface area and total pore volume as well as a smaller mean pore size. It has been proven that larger specific surface area increases will be beneficial for the transfer of CH_4 molecules inside the catalyst pores and can promote contact between CH_4 molecules and active sites, enhancing the efficiency of CH_4 oxidation [42]. When the doping amount of Mn increased, the specific surface area increased from 14 $m^2 \cdot g^{-1}$ (Co_3O_4) to 26 $m^2 \cdot g^{-1}$ ($Mn_{0.025}Co_1$), 33 $m^2 \cdot g^{-1}$ ($Mn_{0.05}Co_1$), and 39 $m^2 \cdot g^{-1}$ ($Mn_{0.1}Co_1$).

2.2. Surface Chemical States

The impacts of properties including the surface elemental valance states and oxygen species on the catalytic activities were characterized by XPS. The XPS spectra of Co $2p_{3/2}$ (Figure 3a) can be divided into two peaks, with which the peak with a binding energy (BE) of 779.4–780.1 eV can be attributed to octahedral Co^{3+}, while the other with a higher BE of 780.4–781.1 eV can be assigned to tetrahedral Co^{2+} [43,44]. When the doping amount of Mn increased, the Co^{2+} ratio ($Co^{2+}/(Co^{2+}+Co^{3+})$) value increased at first and then decreased: $Mn_{0.05}Co_1$ (34.89%) > $Mn_{0.025}Co_1$ (32.16%) > $Mn_{0.1}Co_1$ (28.50%) > Co_3O_4 (27.41%), indicating a highest surface Co^{2+} content of $Mn_{0.05}Co_1$. The introduction of a decent amount of Mn into the Co_3O_4 lattice will facilitate the formation of crystal defects such as oxygen vacancy, leading to the reduction of neighbored Co^{3+} ions into Co^{2+}. Excessive Co^{2+} can bring about a surface charge imbalance, causing other metal components to shift from a lower valence state to a higher valence state [45]. This further stimulates the redox balance between Co ions and Mn ions, in which the doping of a decent amount of Mn can effectively facilitate the breakage of Co–O bonds and create more oxygen vacancies [46].

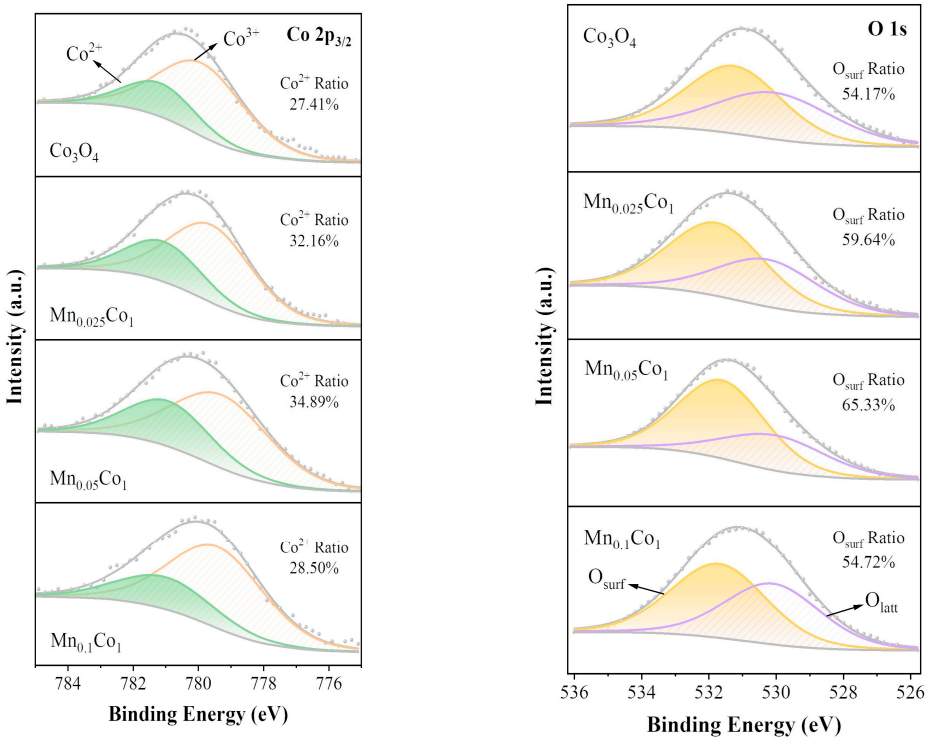

Figure 3. XPS spectra for (**a**) Co $2p_{3/2}$, (**b**) O 1s of Co_3O_4, $Mn_{0.025}Co_1$, $Mn_{0.05}Co_1$, and $Mn_{0.1}Co_1$ catalysts.

Moreover, the deconvolution of O 1s XPS spectra with two subpeaks is represented in Figure 3b, in which the peaks at 530.8 eV and 529.6 eV can be assigned to the surface-active oxygen species (O_{surf}, e.g., O_2^-, O^-, and O_2^{2-}) associated with the oxygen vacancies

and the lattice oxygen (O_{latt}, e.g., O^{2-}), respectively [47]. O_{surf} is the active oxygen species in catalytic oxidation [48]. The formation of active O_{surf} is related to the generation of oxygen vacancies, which is conducive to the adsorption and activation of oxygen molecules [49–51]. As a result, when the doping amount of Mn increases, the O_{surf} ratio ($O_{surf}/(O_{surf}+O_{latt})$) value increases at first—from 54.17% (Co_3O_4) to 65.33% ($Mn_{0.05}Co_1$)—and then decreases, suggesting a superior catalytic activity of the $Mn_{0.05}Co_1$ catalyst when compared to other Mn-Co_3O_4 catalysts. After being consumed by the oxidation of methane and intermediates, the dissipative surface-active oxygen species can be replenished by the migration of the bulk lattice oxygen species and the supplement of the gaseous O_2, following the MvK mechanism [21,38]. The active oxygen species released from Co_3O_4 due to the reduction of Co^{3+} will transfer to the Mn species, benefiting the redox reaction cycle ($Co^{3+} + Mn^{3+} \leftrightarrow Co^{2+} + Mn^{4+}$), which is responsible for the improved catalytic performance [28,46].

2.3. Redox Capabilities

The redox capacities of different catalysts are characterized by H_2-TPR (Figure 4). The spectrum of pure Co_3O_4 mainly consists of two reducing peaks, in which the peak at 250–400 °C is attributed to the reduction of Co_3O_4 to CoO, while the peak at 370–500 °C to the reduction of CoO to Co^0 [52–54]. The spectrum of pure MnO_x mainly consists of two reducing peaks (300–350 °C and 400–450 °C) as well, which are attributed to the reduction of highly-dispersed MnO_2 and Mn^{3+} to Mn^{2+}, respectively [40,54,55]. The internal reduction temperatures of Co and Mn oxides are rather close, and thus it is difficult to thoroughly split their respective reducing peaks apart [40,54]. The first peak of $Mn_{0.05}Co_1$ at 328 °C can be assigned to the combined reduction of Co^{3+} and Mn^{4+} to Co^{2+} and Mn^{3+}, the second peak at 401 °C is attributed to the continuous combined reduction of Co^{2+} and Mn^{3+}, while the third peak at 503 °C is attributed to the reduction of Co^{2+} to Co^0. When Mn is doped into Co_3O_4, both the first and second reducing peaks of Mn_xCo_1 (x = 0.025, 0.05, and 0.1) are shifted to lower temperatures, indicating the improvement in the redox capacity, which is beneficial for the CMC process. Combined with the previous results, we suggest that Mn doping can increase the number of oxygen vacancies and active oxygen species, and the oxygen mobility can be correspondingly enhanced, thus causing the reduction profiles to shift to lower temperatures. However, when the Mn doping amount is further increased from 5.0% to 10.0%, the areas of the reduction peaks decrease significantly, indicating the decreased content of oxygen vacancies and surface active oxygen species, which is consistent with the XPS results. The above results show that the redox capacity of $Mn_{0.05}Co_1$ can be improved by Mn doping, which can promote the redox cycles among the reducible Mn–Co species.

To further study the oxygen properties and verify the mobility of oxygen, O_2-TPD experiments of Co_3O_4 and Mn_xCo_1 catalysts were performed, and the results are shown in Figure 5. For all the samples, oxygen desorption peaks appeared at about 600 °C, which can be attributed to lattice oxygen species released from the Co_3O_4 bulk [56,57]. Pure Co_3O_4 has a small oxygen desorption peak with a center temperature of 667 °C. After doping a decent amount of manganese into Co_3O_4, the desorption temperatures of the composite oxides significantly decreased, indicating the improved oxygen mobility of Mn_xCo_1. Moreover, $Mn_{0.05}Co_1$ exhibited the lowest O_2 desorption temperature at 570 °C, then the desorption temperature rose to 580 °C when the doping amount of manganese was further increased to 0.1, demonstrating that active oxygen vacancies most easily formed on $Mn_{0.05}Co_1$, which agrees with the XPS results. Based on the above investigations, it can be estimated that the doping of Mn into the Co_3O_4 lattice facilitates the release of lattice oxygen at high temperatures, and significantly enhances the redox capacities and oxygen mobility, which is beneficial to promoting CMC activities.

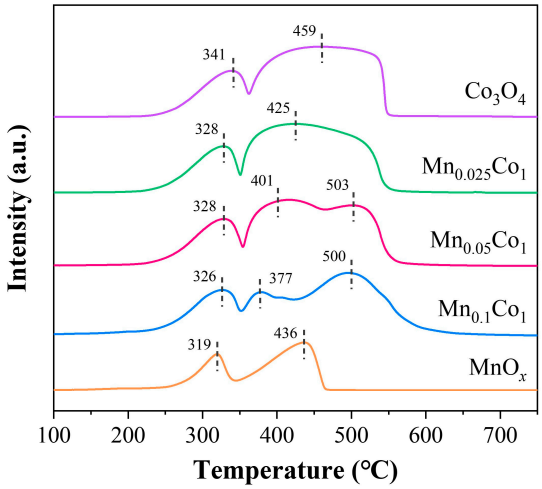

Figure 4. H_2-TPR profiles of Co_3O_4 and Mn_xCo_1 (x = 0.025, 0.05, 0.1) catalysts.

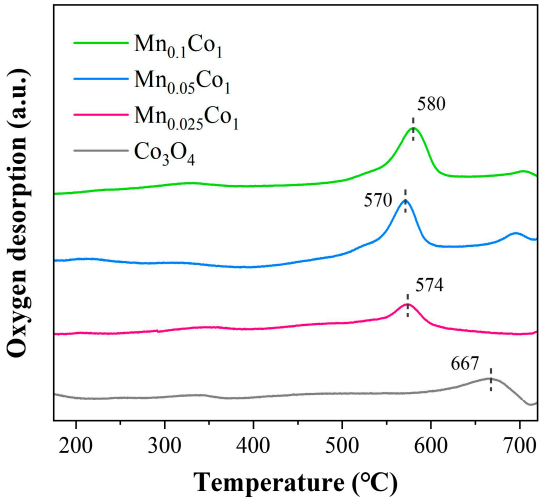

Figure 5. O_2-TPD profiles of the Co_3O_4 and Mn_xCo_1 (x = 0.025, 0.05, 0.1) catalysts.

2.4. Catalytic Performance for Low-Concentration CH_4 Combustion

The CMC catalytic activities of different catalysts were evaluated (Figure 6) including Mn-doped Co_3O_4 with different doping amounts, pure Co_3O_4, and MnO_x. The Mn doping amounts in the Mn-Co_3O_4 samples were 2.5%, 5.0%, 10.0%, and 20.0%, respectively. As shown in Figure 6a, among all of the tested catalysts, pure MnO_x showed a low activity for CMC, in which the temperature needed for 50% conversion of CH_4 (T_{50}) was over 408 °C. On the other hand, pure Co_3O_4 had good activity, in which T_{50} was about 333 °C, indicating that in the whole system, Co_3O_4 plays a major role in CH_4 catalytic oxidation. When small amounts of Mn were doped into Co_3O_4, the low-concentration CMC catalytic performances of the obtained Mn-Co_3O_4 samples were improved to a certain extent. When the doping amount of Mn was increased from 2.5% to 20.0%, the catalytic activity first increased and then decreased. When the doping amount of Mn increased to 20.0%, the activity of $Mn_{0.2}Co_1$ was much lower than that of Co_3O_4, indicating that manganese is no longer easily incorporated into the Co_3O_4 lattice to form a Mn–Co solid solution at this time, but mainly exists in the form of aggregated Mn_2O_3 oxide, as shown in the XRD pattern of Figure S3. From the experimental results, the $Mn_{0.05}Co_1$ catalyst with the Mn doping amount of 5.0% had the best activity, in which T_{50} and T_{90} (the temperature needed for 90% CH_4 conversion) were 310 °C and 370 °C, respectively. It can be concluded that doping the proper amount of Mn is beneficial to improving the catalytic performance of Co_3O_4.

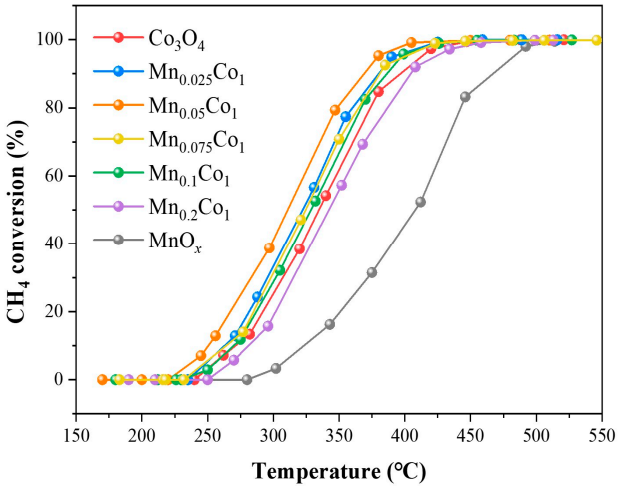

(**a**)

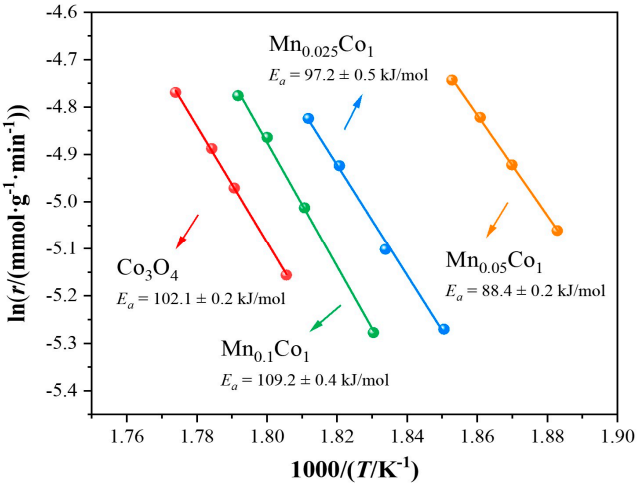

(**b**)

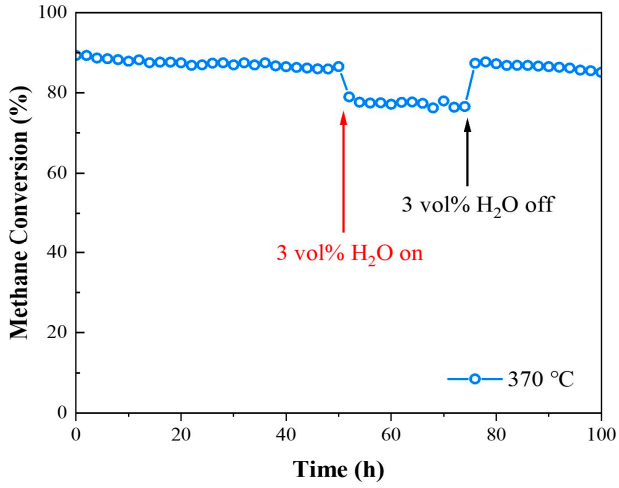

(**c**)

Figure 6. (**a**) Catalytic activities of the Co_3O_4, Mn-doped Co_3O_4, and MnO_x samples. (**b**) Arrhenius plots of the CH_4 oxidation rates over the Co_3O_4 and Mn_xCo_1 (x = 0.025, 0.05, 0.1) catalysts. (**c**) Stability test and effect of 3 vol% steam on CH_4 conversion over the $Mn_{0.05}Co_1$ catalyst at 370 °C. Reaction conditions: 0.5 vol% CH_4, 20 vol% O_2, N_2 as the balance gas. GHSV = 12,000 mL g^{-1} h^{-1}.

To compare the catalytic activity differences of the samples more clearly, the temperatures needed for 10%, 50%, and 90% CH_4 conversion (T_{10}, T_{50}, and T_{90}) of all the catalysts as well as their reaction rates per unit area per second at 250 °C are summarized in Table 2. The reaction rates per unit area per second of the relevant catalysts were calculated on the activity data of a CH_4 conversion lower than 20%. The Arrhenius equations for CMC reactions of Co_3O_4, $Mn_{0.025}Co_1$, $Mn_{0.05}Co_1$, and $Mn_{0.1}Co_1$ catalysts were calculated according to their reaction rates (Figure 6b). The apparent activation energy of CH_4 oxidation was determined by the slope of the Arrhenius equation, and for the above catalysts, the activation energies were $Mn_{0.1}Co_1$ (109.2 ± 0.4 kJ·mol^{-1}) > Co_3O_4 (102.1 ± 0.2 kJ·mol^{-1}) > $Mn_{0.025}Co_1$ (97.2 ± 0.5 kJ·mol^{-1}) > $Mn_{0.05}Co_1$ (88.4 ± 0.2 kJ·mol^{-1}), which was consistent with the CMC reaction results. This further proves that the $Mn_{0.05}Co_1$ catalyst with a small Mn doping amount had the highest catalytic activity. It can be concluded that the formation of the Mn–Co solid solution and the increase in the redox pairs of the Co/Mn multi-valence ions can effectively improve the oxygen mobility and increase oxygen vacancies. Although the specific surface area of the $Mn_{0.05}Co_1$ catalyst increases due to manganese incorporation, the more essential reasons for its performance enhancements were the higher oxygen mobility and more oxygen vacancies.

Table 2. Catalytic activities over the Co_3O_4, Mn_xCo_1 (x = 0.025, 0.05, and 0.1), and MnO_x catalysts.

Catalysts	T_{10} (°C)	T_{50} (°C)	T_{90} (°C)	r [1] × 10^9 (mol·m^{-2}·s^{-1})
Co_3O_4	269	333	395	1.57
$Mn_{0.025}Co_1$	262	321	379	1.63
$Mn_{0.05}Co_1$	250	310	370	2.14
$Mn_{0.1}Co_1$	269	328	385	0.66
MnO_x	323	408	468	0.06

[1] The feed gas was 0.5 vol% CH_4 and 20 vol% O_2/N_2 at T = 250 °C.

On the other hand, the CMC stability test for the $Mn_{0.05}Co_1$ catalyst with the best performance was carried out at 370 °C (Figure 6c). After continuous reaction for 100 h, the CH_4 conversion was maintained at above 85%, expressing good durability, which provides the potential possibility for its application in the CH_4 treatment industry. To further investigate the water resistance, water vapor (3 vol%) was further introduced after 50 h. The CH_4 conversion of $Mn_{0.05}Co_1$ first decreased from 86.6% to 79% and then fluctuated in the range of 76–78% for 25 h. When the vapor was evacuated, the activity of the $Mn_{0.05}Co_1$ catalyst could be thoroughly recovered to the initial level, giving a CH_4 conversion of 87.4% again, which could be maintained above 85% in the next 25 h of operation. It was found that the methane conversion could quickly increase to the previous level after stopping the water addition and still showed good stability. Based on the above results, we can conclude that the introduction of steam had a certain effect on the CMC reactivity of the $Mn_{0.05}Co_1$ sample, but this effect is reversible because its activity can be recovered after the water is removed, illustrating that the $Mn_{0.05}Co_1$ catalyst has a certain degree of water resistance.

2.5. In Situ DRIFTS Study

The CH_4 adsorption processes at room temperature on the $Mn_{0.05}Co_1$ and Co_3O_4 catalysts over time were observed by in situ DRIFTS spectra (Figure 7a,b). The peaks at 3016 cm^{-1} and 1304 cm^{-1} were attributed to the C–H vibration of CH_4, while the peak near 1613 cm^{-1} was attributed to the antisymmetric stretching vibrations of formates (HCO or HCOO) [58–60]. For $Mn_{0.05}Co_1$, the formate species can be instantly well-observed after introducing the CH_4 stream for 1 min, while the intensities of the same peaks on Co_3O_4 are very weak, indicating that the CH_4 molecules are more easily oxidized by the surface-active lattice oxygen on the $Mn_{0.05}Co_1$ surface under O_2-free circumstances, which obey the fundamental properties of the MvK mechanism. Furthermore, the surface-active lattice

oxygen on $Mn_{0.05}Co_1$ is more reactive than that on Co_3O_4. For a more visual comparison of the CH_4 relative adsorption capacity, the peak signals of $Mn_{0.05}Co_1$ and Co_3O_4 after 15-min of CH_4 adsorption were compared under the same testing conditions after weighing the same amount of samples accurately (Figure S4). $Mn_{0.05}Co_1$ had a higher maximum peak intensity than Co_3O_4, suggesting that more CH_4 was absorbed on $Mn_{0.05}Co_1$, which had a higher surface CH_4 adsorption capacity.

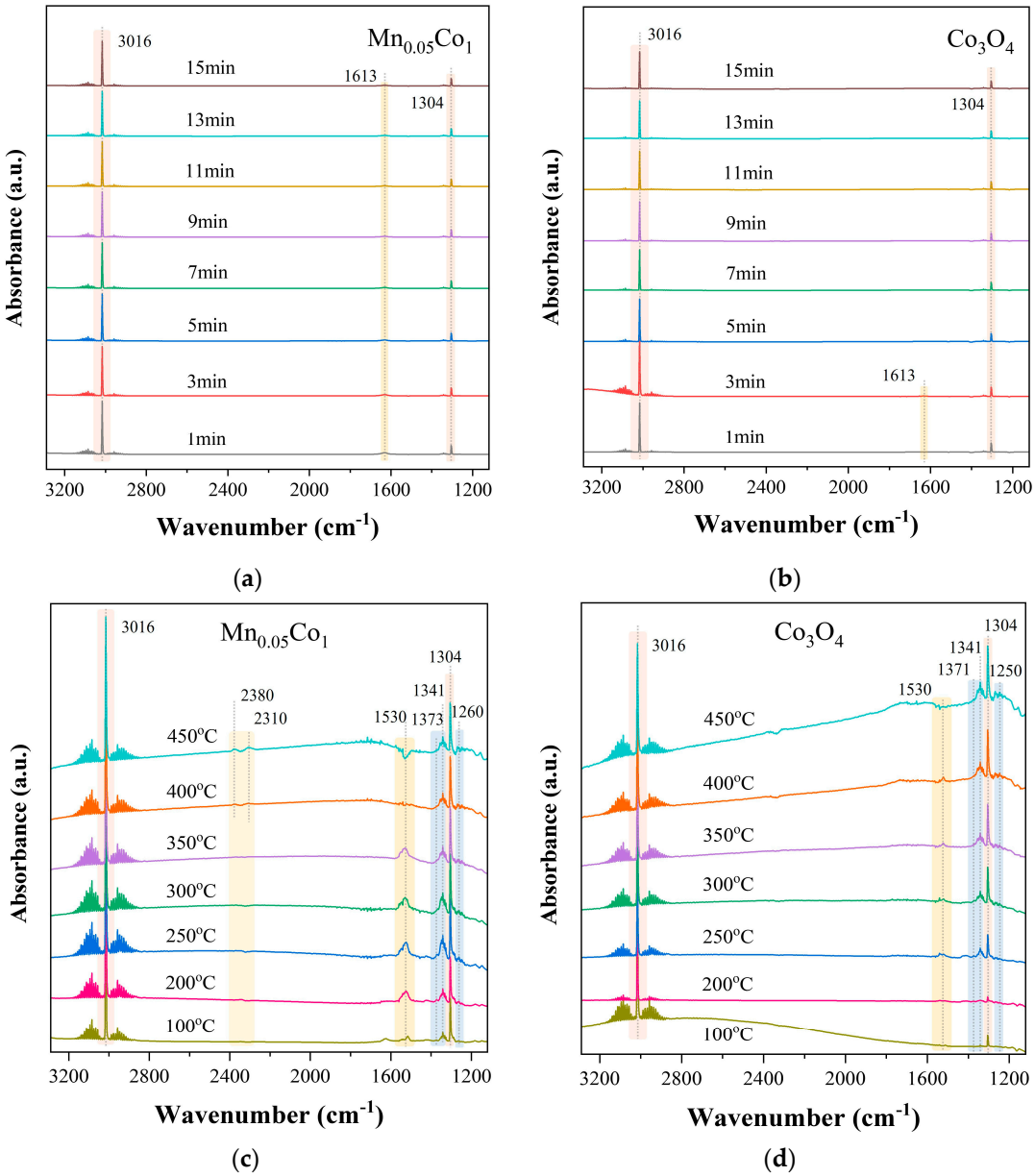

Figure 7. In situ DRIFTS spectra of CH_4 adsorption over the (**a**) $Mn_{0.05}Co_1$ and (**b**) Co_3O_4 catalysts as a function of time at 30 °C, and the in situ DRIFTS spectra with the temperature increased after CH_4 + O_2 adsorption over the (**c**) $Mn_{0.05}Co_1$ and (**d**) Co_3O_4 catalysts.

Moreover, the in situ DRIFTS spectra of the $Mn_{0.05}Co_1$ and Co_3O_4 catalysts with a temperature rise in an atmosphere of 1% CH_4 + O_2 were characterized (Figure 7c,d) to identify the intermediate species and their contents changed during CH_4 oxidation. For $Mn_{0.05}Co_1$, the peak at 1530 cm^{-1} was attributed to formates, while the peaks at 1373 cm^{-1}, 1341 cm^{-1}, and 1260 cm^{-1} were attributed to carbonates. For Co_3O_4, the peak at 1530 cm^{-1} was attributed to formates, while the peaks at 1371 cm^{-1}, 1341 cm^{-1}, and 1250 cm^{-1} were attributed to carbonates [59–61]. At low temperatures (100–350 °C), a certain amount of formate and

carbonate intermediates were detected for $Mn_{0.05}Co_1$, while almost no intermediates were detected at the same temperature for Co_3O_4. Merely a small number of formates and carbonates were detected on the Co_3O_4 surface with an increase in temperature to 250 °C. On the other hand, at high temperatures (350–450 °C), the intensity of the formate peak signals on the $Mn_{0.05}Co_1$ surface weakened as the temperature increased, and due to the fast reaction depletion at 400 °C, the formate peaks almost disappeared. At the same time, the peaks at 2300–2400 cm^{-1} could be observed at 450 °C, which were attributed to the C=O stretch of the vibration of gaseous CO_2. This means that the intermediates undergo rapid conversion and are more likely to further oxidize into carbonates and the product CO_2 on the $Mn_{0.05}Co_1$ surface [62]. The above results indicate that $Mn_{0.05}Co_1$ has a stronger capacity for CH_4 and O_2 activation, assisting in the production of intermediates and CO_2. This is one of the significant reasons for the CMC performance difference between the two catalysts.

3. Materials and Methods

3.1. Catalyst Preparation

Basic cobalt carbonate ($(CoCO_3)_2{\cdot}[Co(OH)_2]_3{\cdot}xH_2O$, 99%) was purchased from Sinopharm (Shanghai, China). Manganese carbonate ($MnCO_3$, 99%) was purchased from Aladdin (Shanghai, China). A series of improved catalysts of Mn-doped Co_3O_4 with different doping amounts was synthesized by the solid-state reactions of basic cobalt carbonate and manganese carbonate. In the synthesis procedure, the scaled carbonate precursors were placed in the grinding jar, in which the grinding media of zirconium oxide balls occupied a 1/3 of the whole volume. The precursors were then ground and mixed at room temperature for 8 h using a planetary ball mill at a speed of 200 rpm. The doping amount of Mn was adjusted at the range of 2.5–20.0 mol% than that of Co. The obtained powder was dried overnight at 110 °C and then calcined at 550 °C for 4 h. The obtained mixture after calcination is denoted as Mn_xCo_1, in which x stands for the molar ratio of Mn/Co. The reference catalysts of pure MnO_x and Co_3O_4 samples were synthesized according to the same procedure using basic cobalt carbonate and manganese carbonate, respectively.

3.2. Catalyst Characterizations

X-ray powder diffraction (XRD) was carried out on a Bruker AXS D8 diffractometer (AXS D8, Bruker, Madison, WI, USA). The XRD spectra were obtained in the 2θ of 10–80° to identify the crystal structures of the calcinated samples. The micromorphology of the catalysts was observed by field-emission scanning electron microscopy (FESEM) and high-resolution transmission electron microscopy (HRTEM). FESEM images were obtained on a Gemini 500 microscope (Gemini 500, Zeiss, Oberkochen, Ostalbkreis, Baden-Württemberg, Germany) at a working voltage of 3 kV. HRTEM images were obtained on a Tecnai G2 F20 S-Twin microscope (Tecnai G2 F20 S-Twin, FEI, Waltham, MA, USA) at a working voltage of 200 kV. The specific surface areas (SSA), pore volumes, and pore distributions were characterized by nitrogen adsorption–desorption isotherms on a Quadrasorb evo analyzer (Quadrasorb evo, Quantachrome, Boynton Beach, FL, USA). The pore structure data were then calculated according to the Brunauer–Emmett–Teller (BET) equation and the Barrett–Joyner–Halenda (BJH) model (Quadrasorb evo, Quantachrome, Boynton Beach, FL, USA). X-ray photoelectronic spectroscopy (XPS) was carried out on a PHI 5000C spectrometer (PHI 5000C, ULVCA-PHI, Chanhassen, MN, USA) to identify the surface element composition, valence states, and content of the catalysts. The reductivity and oxygen mobility of the catalysts were characterized by hydrogen temperature-programmed reduction (H_2-TPR) and oxygen temperature-programmed desorption (O_2-TPD) on a ChemiSorb 2720 automatic multi-purpose adsorption instrument (Auto Chem II 2720, Micromeritics, Norcross, GA, USA). Before the H_2-TPR experiments, the 40–60-mesh sample of 100 mg was filled in a quartz tube and pretreated under helium (flow rate

30 mL·min^{-1}) at 200 °C for 2 h (heating rate 10 °C·min^{-1}). The sample was then cooled to room temperature under a helium atmosphere. After that, the sample was heated under 10% H_2/Ar to 800 °C (heating rate 10 °C·min^{-1}), during which the curve was recorded. In the O_2-TPD experiments, the 40–60-mesh sample of 100 mg was pretreated under 5% O_2/He (flow rate 30 mL·min^{-1}) at 300 °C for 1 h (heating rate 10 °C·min^{-1}). After that, the sample was purged using helium for 0.5 h at 300 °C and then heated to 800 °C with a heating rate of 10 °C·min^{-1}, during which the curve was recorded. In situ diffuse reflectance infrared Fourier transform spectroscopy (in situ DRIFTS) was carried out on a Nicolet 6700 spectrometer (Nicolet 6700, Thermo Fisher Scientific, Waltham, MA, USA). Before the experiments, the catalyst was pretreated at 300 °C for 1 h and cooled to 30 °C under helium to obtain the background spectrum. The pre-obtained background spectrum at the respective temperature was deducted in the following adsorption/desorption and transient reaction experiments.

3.3. Evaluation of the Catalytic Performance

To evaluate the catalytic activity for the CMC reaction at atmospheric pressure, CMC catalytic experiments toward low-concentration CH_4 were carried out on a fixed-bed reactor. The as-made powder was tablet pressed and sieved (40–60 mesh), and 200 mg of the obtained particles were packed in a quartz tube (inner diameter 4.5 mm). The total flow rate of the feeding gas (0.5 vol% CH_4, and 20 vol% O_2 with N_2 balanced) was 40 mL·min^{-1}, and the gas hourly space velocity (GHSV) was 12,000 mL g^{-1} h^{-1}. The reaction products were detected and analyzed online by the FTD detector of a Thermo trace GC Ultra gas chromatography. The CH_4 conversion (X_{CH_4}) was calculated by the following formula:

$$X_{CH_4}(\%) = \frac{[CH_4]_{in} - [CH_4]_{out}}{[CH_4]_{in}} \times 100\% \quad (1)$$

where $[CH_4]_{in}$ and $[CH_4]_{out}$ are the inlet and outlet CH_4 concentrations at the steady state, respectively.

The CMC reaction rates per unit area per second of the catalysts can be calculated by the following formulas:

$$r(mol \cdot m^{-2} \cdot s^{-1}) = \frac{X_{CH_4} \cdot q \cdot [CH_4]_{in}}{V_m \cdot W \cdot S} \quad (2)$$

$$\ln r = \frac{-E_a}{RT} + C \quad (3)$$

where q, V_m, W, S, E_a, R, and T are the volume flow rate (40 mL·min^{-1}), the standard molar volume of gases (22.4 mL·mmol^{-1}), catalyst mass (0.2 g), SSA of the catalyst (m^2·g^{-1}), activation energy (kJ·mol^{-1}), universal gas constant (8.314 J·mol^{-1}·K^{-1}), and thermodynamic temperature (K), respectively.

4. Conclusions

In summary, a series of Mn-Co_3O_4 catalysts with different Mn doping amounts synthesized by a solid-state method was applied for catalytic methane combustion. The XRD and XPS results revealed that the formation of a Co–Mn solid solution could introduce more crystal defects and oxygen vacancies, inducing higher surface concentrations of Co^{2+} and active oxygen species. The study of H_2-TPR and O_2-TPD analysis indicated the enhancement in redox capacity and oxygen mobility due to more active oxygen vacancies. Compared with the pure Co_3O_4, the $Mn_{0.05}Co_1$ sample exhibited superior catalytic performance in low-concentration methane combustion. The T_{50} and T_{90} of $Mn_{0.05}Co_1$ were 310 and 370 °C, respectively, which is outstanding as a transition metal catalyst compared with other components. Furthermore, the $Mn_{0.05}Co_1$ catalyst also possessed good stability and water resistance (3 vol.% steam). In situ DRIFTS results confirmed that $Mn_{0.05}Co_1$ held

stronger capabilities for CH_4 adsorption and provided more abundant active oxygen species for the reaction, which helped to improve the reaction rates and catalytic performance. It can be concluded that the $Mn_{0.05}Co_1$ catalyst not only had a lower cost than noble metal materials, but also had a good performance in the catalytic combustion reaction of low-concentration methane, making it of great research value and industrial application potential. Based on these results, we propose an effective strategy to develop promising high-performance non-noble metal catalysts for low-concentration methane combustion.

Supplementary Materials: The following supporting information can be downloaded at: https://www.mdpi.com/article/10.3390/catal13030529/s1, Figure S1: N_2 adsorption–desorption isotherms of Co_3O_4, Mn_xCo_1 (x = 0.025, 0.05, and 0.1) and the MnO_x catalysts; Figure S2: Pore size distribution profiles of (A) Co_3O_4, (B) $Mn_{0.025}Co_1$, (C) $Mn_{0.05}Co_1$, (D) $Mn_{0.1}Co_1$, and (E) MnO_x catalysts (Method: BJH desorption); Figure S3: The XRD spectra of the $Mn_{0.2}Co_1$ catalyst; Figure S4: In situ DRIFTS spectra of the $M_{0.05}Co_1$ and Co_3O_4 catalysts after CH_4 adsorption for 15 min.

Author Contributions: Conceptualization, L.X., C.Y., H.X. and W.S.; Methodology, L.X., C.Y., S.W. and Z.H.; Software, L.X. and C.Y.; Validation, C.Y.; Formal analysis, L.X.; Investigation, L.X., S.W. and Z.H.; Resources, Z.H., H.X. and W.S.; Data curation, C.Y. and S.W.; Writing—original draft preparation, L.X.; Writing—review and editing, L.X., C.Y., Z.H., H.X. and W.S.; Visualization, L.X.; Supervision, Z.Y., S.S., H.X. and W.S.; Project administration, H.X. and W.S.; Funding acquisition, Z.H., H.X. and W.S. All authors have read and agreed to the published version of the manuscript.

Funding: This research was funded by Shanghai Science and Technology Committee (Grant No. 14DZ2273900), and the Solvay (China) Co. Ltd.

Data Availability Statement: The data is included in the article or Supplementary Materials.

Conflicts of Interest: The authors declare no conflicts of interest.

References

1. He, X.; Wallington, T.J.; Anderson, J.E.; Keoleian, G.A.; Shen, W.; De Kleine, R.; Kim, H.C.; Winkler, S. Life-Cycle Greenhouse Gas Emission Benefits of Natural Gas Vehicles. *ACS Sustain. Chem. Eng.* **2021**, *9*, 7813–7823. https://doi.org/10.1021/acssuschemeng.1c01324.
2. Gholami, R.; Smith, K.J. Activity of PdO/SiO_2 catalysts for CH_4 oxidation following thermal treatments. *Appl. Catal. B Environ.* **2015**, *168–169*, 156–163. https://doi.org/10.1016/j.apcatb.2014.12.037.
3. Allen, D. Attributing Atmospheric Methane to Anthropogenic Emission Sources. *Acc. Chem. Res.* **2016**, *49*, 1344–1350. https://doi.org/10.1021/acs.accounts.6b00081.
4. Ercolino, G.; Stelmachowski, P.; Grzybek, G.; Kotarba, A.; Specchia, S. Optimization of Pd catalysts supported on Co_3O_4 for low-temperature lean combustion of residual methane. *Appl. Catal. B Environ.* **2017**, *206*, 712–725. https://doi.org/10.1016/j.apcatb.2017.01.055.
5. de Rivas, B.; López-Fonseca, R.; Jiménez-González, C.; Gutiérrez-Ortiz, J.I. Highly active behaviour of nanocrystalline Co_3O_4 from oxalate nanorods in the oxidation of chlorinated short chain alkanes. *Chem. Eng. J.* **2012**, *184*, 184–192. https://doi.org/10.1016/j.cej.2012.01.027.
6. Zhu, Z.; Lu, G.; Zhang, Z.; Guo, Y.; Guo, Y.; Wang, Y. Highly Active and Stable Co_3O_4/ZSM-5 Catalyst for Propane Oxidation: Effect of the Preparation Method. *ACS Catal.* **2013**, *3*, 1154–1164. https://doi.org/10.1021/cs400068v.
7. Dietl, N.; Schlangen, M.; Schwarz, H. Thermal hydrogen-atom transfer from methane: The role of radicals and spin states in oxo-cluster chemistry. *Angew. Chem. Int. Ed. Engl.* **2012**, *51*, 5544–5555. https://doi.org/10.1002/anie.201108363.
8. Choudhary, T.V.; Banerjee, S.; Choudhary, V.R. Catalysts for combustion of methane and lower alkanes. *Appl. Catal. A Gen.* **2002**, *234*, 1–23.
9. Liotta, L.F.; Wu, H.; Pantaleo, G.; Venezia, A.M. Co_3O_4 nanocrystals and Co_3O_4–MO_x binary oxides for CO, CH_4 and VOC oxidation at low temperatures: A review. *Catal. Sci. Technol.* **2013**, *3*, 3085–3102. https://doi.org/10.1039/c3cy00193h.
10. Kim, S.C.; Shim, W.G. Catalytic combustion of VOCs over a series of manganese oxide catalysts. *Appl. Catal. B Environ.* **2010**, *98*, 180–185. https://doi.org/10.1016/j.apcatb.2010.05.027.
11. Huang, Z.; Wei, Y.; Song, Z.; Luo, J.; Mao, Y.; Gao, J.; Zhang, X.; Niu, C.; Kang, H.; Wang, Z. Three-dimensional (3D) hierarchical Mn_2O_3 catalysts with the highly efficient purification of benzene combustion. *Sep. Purif. Technol.* **2021**, *255*, 117633. https://doi.org/10.1016/j.seppur.2020.117633.
12. Ji, J.; Lu, X.; Chen, C.; He, M.; Huang, H. Potassium-modulated δ-MnO_2 as robust catalysts for formaldehyde oxidation at room temperature. *Appl. Catal. B Environ.* **2020**, *260*, 118210. https://doi.org/10.1016/j.apcatb.2019.118210.
13. Wang, F.; Dai, H.; Deng, J.; Bai, G.; Ji, K.; Liu, Y. Manganese oxides with rod-, wire-, tube-, and flower-like morphologies: Highly effective catalysts for the removal of toluene. *Environ. Sci. Technol.* **2012**, *46*, 4034–4041. https://doi.org/10.1021/es204038j.

14. Li, G.; Zhang, C.; Wang, Z.; Huang, H.; Peng, H.; Li, X. Fabrication of mesoporous Co_3O_4 oxides by acid treatment and their catalytic performances for toluene oxidation. *Appl. Catal. A Gen.* **2018**, *550*, 67–76. https://doi.org/10.1016/j.apcata.2017.11.003.
15. Zhang, X.; Wei, Y.; Song, Z.; Liu, W.; Gao, C.; Luo, J. Silicotungstic acid modified CeO_2 catalyst with high stability for the catalytic combustion of chlorobenzene. *Chemosphere* **2021**, *263*, 128129. https://doi.org/10.1016/j.chemosphere.2020.128129.
16. Wang, H.; Guo, W.; Jiang, Z.; Yang, R.; Jiang, Z.; Pan, Y.; Shangguan, W. New insight into the enhanced activity of ordered mesoporous nickel oxide in formaldehyde catalytic oxidation reactions. *J. Catal.* **2018**, *361*, 370–383. https://doi.org/10.1016/j.jcat.2018.02.023.
17. Cai, T.; Yuan, J.; Zhang, L.; Yang, L.; Tong, Q.; Ge, M.; Xiao, B.; Zhang, X.; Zhao, K.; He, D. Ni–Co–O solid solution dispersed nanocrystalline Co_3O_4 as a highly active catalyst for low-temperature propane combustion. *Catal. Sci. Technol.* **2018**, *8*, 5416–5427. https://doi.org/10.1039/c8cy01062e.
18. Castaño, M.H.; Molina, R.; Moreno, S. Cooperative effect of the Co–Mn mixed oxides for the catalytic oxidation of VOCs: Influence of the synthesis method. *Appl. Catal. A Gen.* **2015**, *492*, 48–59. https://doi.org/10.1016/j.apcata.2014.12.009.
19. Hu, Z.; Qiu, S.; You, Y.; Guo, Y.; Guo, Y.; Wang, L.; Zhan, W.; Lu, G. Hydrothermal synthesis of $NiCeO_x$ nanosheets and its application to the total oxidation of propane. *Appl. Catal. B Environ.* **2018**, *225*, 110–120. https://doi.org/10.1016/j.apcatb.2017.08.068.
20. Luo, M.; Cheng, Y.; Peng, X.; Pan, W. Copper modified manganese oxide with tunnel structure as efficient catalyst for low-temperature catalytic combustion of toluene. *Chem. Eng. J.* **2019**, *369*, 758–765. https://doi.org/10.1016/j.cej.2019.03.056.
21. Zhang, X.; Zhao, M.; Song, Z.; Zhao, H.; Liu, W.; Zhao, J.; Ma, Z. a.; Xing, Y. The effect of different metal oxides on the catalytic activity of a Co_3O_4 catalyst for toluene combustion: Importance of the structure–property relationship and surface active species. *New J. Chem.* **2019**, *43*, 10868–10877. https://doi.org/10.1039/c9nj01783f.
22. Chen, L.; Jia, J.; Ran, R.; Song, X. Nickel doping MnO_2 with abundant surface pits as highly efficient catalysts for propane deep oxidation. *Chem. Eng. J.* **2019**, *369*, 1129–1137. https://doi.org/10.1016/j.cej.2019.03.142.
23. Pu, Z.; Zhou, H.; Zheng, Y.; Huang, W.; Li, X. Enhanced methane combustion over Co_3O_4 catalysts prepared by a facile precipitation method: Effect of aging time. *Appl. Surf. Sci.* **2017**, *410*, 14–21. https://doi.org/10.1016/j.apsusc.2017.02.186.
24. Zheng, Y.; Liu, Y.; Zhou, H.; Huang, W.; Pu, Z. Complete combustion of methane over Co_3O_4 catalysts: Influence of pH values. *J. Alloys Compd.* **2018**, *734*, 112–120. https://doi.org/10.1016/j.jallcom.2017.11.008.
25. El-Shobaky, H.G.; Shouman, M.A.; Attia, A.A. Effect of La_2O_3 and Mn_2O_3-doping of Co_3O_4/Al_2O_3 system on its surface and catalytic properties. *Collids Surf. A* **2006**, *274*, 62–70. https://doi.org/10.1016/j.colsurfa.2005.08.035.
26. Tang, X.; Gao, F.; Xiang, Y.; Yi, H.; Zhao, S. Low temperature catalytic oxidation of nitric oxide over the Mn–CoO_x catalyst modified by nonthermal plasma. *Catal. Commun.* **2015**, *64*, 12–17. https://doi.org/10.1016/j.catcom.2015.01.027.
27. Wu, M.; Zhan, W.; Guo, Y.; Guo, Y.; Wang, Y.; Wang, L.; Lu, G. An effective Mn–Co mixed oxide catalyst for the solvent-free selective oxidation of cyclohexane with molecular oxygen. *Appl. Catal. A Gen.* **2016**, *523*, 97–106. https://doi.org/10.1016/j.apcata.2016.06.001.
28. Chang, T.; Shen, Z.; Huang, Y.; Lu, J.; Ren, D.; Sun, J.; Cao, J.; Liu, H. Post-plasma-catalytic removal of toluene using MnO_2–Co_3O_4 catalysts and their synergistic mechanism. *Chem. Eng. J.* **2018**, *348*, 15–25. https://doi.org/10.1016/j.cej.2018.04.186.
29. du Preez, S.P.; Bessarabov, D.G. The effects of bismuth and tin on the mechanochemical processing of aluminum-based composites for hydrogen generation purposes. *Int. J. Hydrogen Energy* **2019**, *44*, 21896–21912. https://doi.org/10.1016/j.ijhydene.2019.06.154.
30. Farhang, Y.; Taheri-Nassaj, E.; Rezaei, M. Pd doped $LaSrCuO_4$ perovskite nano-catalysts synthesized by a novel solid state method for CO oxidation and Methane combustion. *Ceram. Int.* **2018**, *44*, 21499–21506. https://doi.org/10.1016/j.ceramint.2018.08.211.
31. Medina, B.; Verdério Fressati, M.G.; Gonçalves, J.M.; Bezerra, F.M.; Pereira Scacchetti, F.A.; Moisés, M.P.; Bail, A.; Samulewski, R.B. Solventless preparation of Fe_3O_4 and Co_3O_4 nanoparticles: A mechanochemical approach. *Mater. Chem. Phys.* **2019**, *226*, 318–322. https://doi.org/10.1016/j.matchemphys.2019.01.043.
32. Akbari, E.; Alavi, S.M.; Rezaei, M.; Larimi, A. Barium promoted manganese oxide catalysts in low-temperature methane catalytic combustion. *Int. J. Hydrogen Energy* **2021**, *46*, 5181–5196. https://doi.org/10.1016/j.ijhydene.2020.11.016.
33. Amol, P.; Amrute, Z.Ł., Hannah Schreyer, Claudia Weidenthaler, Ferdi Schüth. High-surface-area corundum by mechanochemically induced phase transformation of boehmite. *Science* **2019**, *366*, 485–489.
34. Tang, W.; Xiao, W.; Wang, S.; Ren, Z.; Ding, J.; Gao, P.-X. Boosting catalytic propane oxidation over PGM-free Co_3O_4 nanocrystal aggregates through chemical leaching: A comparative study with Pt and Pd based catalysts. *Appl. Catal. B Environ.* **2018**, *226*, 585–595. https://doi.org/10.1016/j.apcatb.2017.12.075.
35. Chen, L.; Hu, J.; Richards, R.; Prikhodko, S.; Kodambaka, S. Synthesis and surface activity of single-crystalline Co_3O_4 (111) holey nanosheets. *Nanoscale* **2010**, *2*, 1657–1660. https://doi.org/10.1039/c0nr00205d.
36. Jiang, Y.; Wu, Y.; Xie, B. Moderate temperature synthesis of nanocrystalline Co_3O_4 via gel hydrothermal oxidation. *Mater. Chem. Phys.* **2002**, *74*, 234–237.
37. Zhai, G.; Wang, J.; Chen, Z.; An, W.; Men, Y. Boosting soot combustion efficiency of Co_3O_4 nanocrystals via tailoring crystal facets. *Chem. Eng. J.* **2018**, *337*, 488–498. https://doi.org/10.1016/j.cej.2017.12.141.
38. Solsona, B.; Vázquez, I.; Garcia, T.; Davies, T.E.; Taylor, S.H. Complete oxidation of short chain alkanes using a nanocrystalline cobalt oxide catalyst. *Catal. Lett.* **2007**, *116*, 116–121. https://doi.org/10.1007/s10562-007-9136-3.

39. Ma, J.; Wang, C.; He, H. Transition metal doped cryptomelane-type manganese oxide catalysts for ozone decomposition. *Appl. Catal. B Environ.* **2017**, *201*, 503–510. https://doi.org/10.1016/j.apcatb.2016.08.050.
40. Todorova, S.; Kolev, H.; Holgado, J.P.; Kadinov, G.; Bonev, C.; Pereñíguez, R.; Caballero, A. Complete n-hexane oxidation over supported Mn–Co catalysts. *Appl. Catal. B Environ.* **2010**, *94*, 46–54. https://doi.org/10.1016/j.apcatb.2009.10.019.
41. Zheng, Y.; Wang, W.; Jiang, D.; Zhang, L. Amorphous MnO_x modified Co_3O_4 for formaldehyde oxidation: Improved low-temperature catalytic and photothermocatalytic activity. *Chem. Eng. J.* **2016**, *284*, 21–27. https://doi.org/10.1016/j.cej.2015.08.137.
42. Qiu, M.; Zhan, S.; Yu, H.; Zhu, D. Low-temperature selective catalytic reduction of NO with NH_3 over ordered mesoporous $Mn_xCo_{3-x}O_4$ catalyst. *Catal. Commun.* **2015**, *62*, 107–111. https://doi.org/10.1016/j.catcom.2015.01.022.
43. Chuang, T.J.; Brundle, C.R.; Rice, D.W. Interpretation of the X-ray photoemission spectra of cobalt oxides and cobalt oxide surfaces. *Surf. Sci.* **1976**, *59*, 413–429.
44. González-Prior, J.; López-Fonseca, R.; Gutiérrez-Ortiz, J.I.; de Rivas, B. Catalytic removal of chlorinated compounds over ordered mesoporous cobalt oxides synthesised by hard-templating. *Appl. Catal. B Environ.* **2018**, *222*, 9–17. https://doi.org/10.1016/j.apcatb.2017.09.050.
45. Luo, Y.; Zheng, Y.; Zuo, J.; Feng, X.; Wang, X.; Zhang, T.; Zhang, K.; Jiang, L. Insights into the high performance of Mn–Co oxides derived from metal-organic frameworks for total toluene oxidation. *J. Hazard. Mater.* **2018**, *349*, 119–127. https://doi.org/10.1016/j.jhazmat.2018.01.053.
46. Li, K.; Xu, D.; Liu, K.; Ni, H.; Shen, F.; Chen, T.; Guan, B.; Zhan, R.; Huang, Z.; Lin, H. Catalytic Combustion of Lean Methane Assisted by Electric Field over Mn_xCo_y Catalysts at Low Temperature. *J. Phys. Chem. C* **2019**, *123*, 10377–10388. https://doi.org/10.1021/acs.jpcc.9b00496.
47. Amri, A.; Duan, X.; Yin, C.-Y.; Jiang, Z.-T.; Rahman, M.M.; Pryor, T. Solar absorptance of copper–cobalt oxide thin film coatings with nano-size, grain-like morphology: Optimization and synchrotron radiation XPS studies. *Appl. Surf. Sci.* **2013**, *275*, 127–135. https://doi.org/10.1016/j.apsusc.2013.01.081.
48. Huang, Z.; Zhao, M.; Luo, J.; Zhang, X.; Liu, W.; Wei, Y.; Zhao, J.; Song, Z. Interaction in LaO_x-Co_3O_4 for highly efficient purification of toluene: Insight into LaO_x content and synergistic effect contribution. *Sep. Purif. Technol.* **2020**, *251*, 117369. https://doi.org/10.1016/j.seppur.2020.117369.
49. Jia, J.; Zhang, P.; Chen, L. Catalytic decomposition of gaseous ozone over manganese dioxides with different crystal structures. *Appl. Catal. B Environ.* **2016**, *189*, 210–218. https://doi.org/10.1016/j.apcatb.2016.02.055.
50. Zhang, X.; Zhao, J.; Song, Z.; Liu, W.; Zhao, H.; Zhao, M.; Xing, Y.; Ma, Z.; Du, H. The catalytic oxidation performance of toluene over the Ce–Mn–O_x catalysts: Effect of synthetic routes. *J Colloid Interface Sci.* **2020**, *562*, 170–181. https://doi.org/10.1016/j.jcis.2019.12.029.
51. Liu, Y.; Zhao, P.; Sun, L.; Feng, N.; Wang, L.; Wan, H.; Guan, G. Surface Modification of Cobalt–Manganese Mixed Oxide and Its Application for Low-Temperature Propane Catalytic Combustion. *ChemistrySelect* **2021**, *6*, 522–531. https://doi.org/10.1002/slct.202004530.
52. Liotta, L.F.; Di Carlo, G.; Pantaleo, G.; Venezia, A.M.; Deganello, G. Co_3O_4/CeO_2 composite oxides for methane emissions abatement: Relationship between Co_3O_4–CeO_2 interaction and catalytic activity. *Appl. Catal. B Environ.* **2006**, *66*, 217–227. https://doi.org/10.1016/j.apcatb.2006.03.018.
53. Puértolas, B.; Smith, A.; Vázquez, I.; Dejoz, A.; Moragues, A.; Garcia, T.; Solsona, B. The different catalytic behaviour in the propane total oxidation of cobalt and manganese oxides prepared by a wet combustion procedure. *Chem. Eng. J.* **2013**, *229*, 547–558. https://doi.org/10.1016/j.cej.2013.06.041.
54. Todorova, S.; Naydenov, A.; Kolev, H.; Holgado, J.P.; Ivanov, G.; Kadinov, G.; Caballero, A. Mechanism of complete n-hexane oxidation on silica supported cobalt and manganese catalysts. *Appl. Catal. A Gen.* **2012**, *413–414*, 43–51. https://doi.org/10.1016/j.apcata.2011.10.041.
55. Zhao, Z.; Bao, T.; Zeng, Y.; Wang, G.; Muhammad, T. Efficient cobalt–manganese oxide catalyst deposited on modified AC with unprecedented catalytic performance in CO preferential oxidation. *Catal. Commun.* **2013**, *32*, 47–51. https://doi.org/10.1016/j.catcom.2012.12.001.
56. Morales, M.R.; Barbero, B.P.; Cadús, L.E. Combustion of volatile organic compounds on manganese iron or nickel mixed oxide catalysts. *Appl. Catal. B Environ.* **2007**, *74*, 1–10. https://doi.org/10.1016/j.apcatb.2007.01.008.
57. Xue, L.; Zhang, C.; He, H.; Teraoka, Y. Catalytic decomposition of N_2O over CeO_2 promoted Co_3O_4 spinel catalyst. *Appl. Catal. B Environ.* **2007**, *75*, 167–174. https://doi.org/10.1016/j.apcatb.2007.04.013.
58. Li, J.; Liang, X.; Xu, S.; Hao, J. Catalytic performance of manganese cobalt oxides on methane combustion at low temperature. *Appl. Catal. B Environ.* **2009**, *90*, 307–312. https://doi.org/10.1016/j.apcatb.2009.03.027.
59. Schmal, M.; Souza, M.; Alegre, V.; Dasilva, M.; Cesar, D.; Perez, C. Methane oxidation–effect of support, precursor and pretreatment conditions–in situ reaction XPS and DRIFT. *Catal. Today* **2006**, *118*, 392–401. https://doi.org/10.1016/j.cattod.2006.07.026.
60. Xiong, J.; Mo, S.; Song, L.; Fu, M.; Chen, P.; Wu, J.; Chen, L.; Ye, D. Outstanding stability and highly efficient methane oxidation performance of palladium-embedded ultrathin mesoporous Co_2MnO_4 spinel catalyst. *Appl. Catal. A Gen.* **2020**, *598*, 117571. https://doi.org/10.1016/j.apcata.2020.117571.
61. Wang, X.; Liu, Y.; Zhang, Y.; Zhang, T.; Chang, H.; Zhang, Y.; Jiang, L. Structural requirements of manganese oxides for methane oxidation: XAS spectroscopy and transition-state studies. *Appl. Catal. B Environ.* **2018**, *229*, 52–62. https://doi.org/10.1016/j.apcatb.2018.02.007.

62. Zhao, S.; Li, K.; Jiang, S.; Li, J. Pd–Co based spinel oxides derived from pd nanoparticles immobilized on layered double hydroxides for toluene combustion. *Appl. Catal. B Environ.* **2016**, *181*, 236–248. https://doi.org/10.1016/j.apcatb.2015.08.001.